



Full Length Article

A Gaussian Decomposition Method and its applications to the prediction of shale gas production

Guanglei Cui^{a,b,c}, Yixin Zhao^{a,b}, Jishan Liu^{d,*}, Mingyao Wei^e, Derek Elsworth^f

^a Beijing Key Laboratory for Precise Mining of Intergrown Energy and Resources, China University of Mining and Technology, Beijing 100083, China

^b College of Resources and Safety Engineering, China University of Mining and Technology, Beijing 100083, China

^c Key laboratory of Ministry of Education on Safe Mining of Deep Metal Mines, Northeastern University, Shenyang 110004, China

^d School of Mechanical and Chemical Engineering, The University of Western Australia, 35 Stirling Highway, Perth, WA 6009, Australia

^e State Key Laboratory of Geomechanics and Geotechnical Engineering, Institute of Rock and Soil Mechanics, Chinese Academy of Sciences, Wuhan 430071, China

^f Department of Energy and Mineral Engineering, G3 Center and Energy Institute, The Pennsylvania State University, University Park, PA 16802, USA

ARTICLE INFO

Keywords:

Gas content
Storage term proportion
Fullscale-coupled experiment
History match
Real-time prediction

ABSTRACT

History matching is normally used to predict the gas production and guide refracturing. This can be achieved either through a mathematics-based approach such as decline curve fitting or through a physics-based approach such as reservoir simulation. When applied to the case of shale gas, both approaches are not working well. In this study, a Gaussian Decomposition Method (GDM), as an alternative approach, is developed and applied to the investigation of shale gas production. In this approach, an auto-compute program is developed and applied to a spectrum of scales from the core scale to the reservoir scale. Specific steps are as follows: (1) we use the experimental measurements to determine the initial gas content distribution; (2) we use the gas production history to decompose the evolving contributions of different gas components in a shale gas reservoir; and (3) we extend the history matching to predict the production of shale gas under similar extraction conditions. For the core scale, we use the automatically decomposed Gaussian components to illustrate the evolving contributions of different gas components including the free-phase gas in pores, the adsorbed gas and the diffused gas to the overall gas production. In the reservoir study, GDM is applied to the production data history matching and real-time prediction. Firstly, GDM is verified against a commercial software on daily, monthly and annual gas production rates. Then a group of daily and monthly field data are history matched by GDM. Finally, GDM is applied to predict the real-time gas production rate. Application results indicate: (a) the early gas production is mainly from big pores/fractures while the late production is from kerogen/clay components; (b) The period of gas production in the early stage is relatively short while the period in the late stage is long.

1. Introduction

The history matching and the real-time prediction of gas rate are the two indispensable processes for the economic evaluation of a well. The history match and real-time prediction methods of unconventional gas production rates inherit from the conventional gas and are categorized into mathematics-based approach and physics-based approach. The mathematics-based approach, traced back to the 1920s [1], uses the curve fitting to match the field data and gains lots of favor because of its easy use. The most popular Arps curves [2] were classified into three types depending on the decline exponent value (b): harmonic decline ($b = 1$), exponential decline ($b = 0$) and hyperbolic decline ($b > 0$ and $b \neq 0$). The traditional mathematics-based approach could bring huge errors when applied to the shale gas well because of the multi-physics,

multi-time and multi-scale flow in shale reservoir [3]. Other mathematical methods, such as Stretched-exponential Decline method [4,5], Power-law Exponential Decline method [6,7] and Duong method [8], are well developed in recent years. However, there are two factors constraining their applications: (1) they have no rigorous theoretical basis which would lead to large uncertainties in prediction; (2) they are not necessarily related to the reservoir property and operating practices; thus, they work better for certain reservoirs but not for all cases [9].

Contrary to the mathematics-based approach, the physics-based approach has strict theoretical explanations establishing a set of Partial Differential Equations (PDEs) to match the bottom hole pressure curve or the gas production data curve. There are two categories of physics-based approach: analytical method and numerical method. For the

* Corresponding author.

E-mail address: jishan.liu@uwa.edu.au (J. Liu).

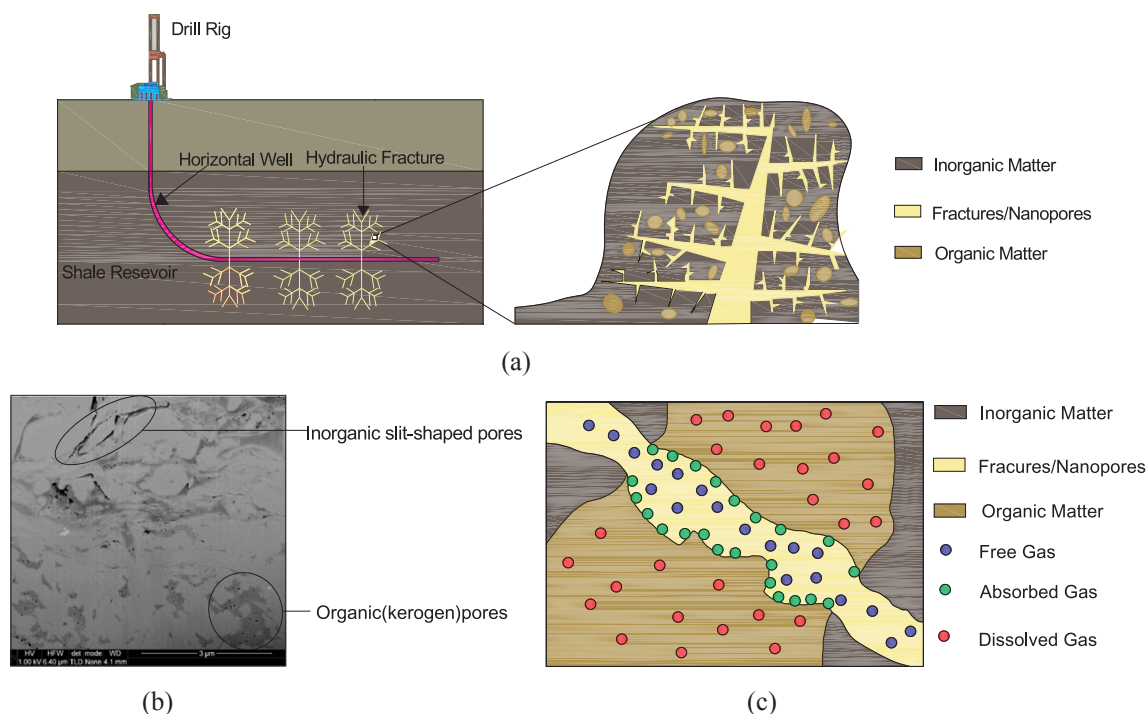


Fig. 1. (a) Schematic illustration of stimulated reservoir volume, (b) SEM image of shale matrix and (c) distribution of gas contents in a controlled volume.

analytical method, the most popular one is the tri-linear flow model. Three linear flow regimes [10,11] are taken into consideration in this method: flow within the fracture, flow within the stimulated region and flow within the un-stimulated region. The analytical method simplifies the reservoir property to search for the analytical solution and the detailed couplings between the gas flow and solid deformation are ignored [12,13]. Moreover, most analytical methods are limited to single-phase flow cases ignoring the impact of water.

The numerical method is popular with the development of computing speed which can be categorized into continuous model and discrete model [14]. For the continuous model, the dual-porosity models and multi-porosity models are widely used [15–18] and in these models the computational nodes on the grid can represent different physical meanings. Take as an example, Yan [19] presented an up-scaled triple permeability simulator for fluid flow in shale reservoirs by capturing the sequential flow in three separate porosity systems: organic matter (mainly kerogen), inorganic matter and natural fractures. For the discrete model, the widely used method is Discrete Fracture Network (DFN) where the fractures are directly modeled and the computational nodes represent either matrix or fracture [20,21]. A DFN model was developed by Doe [22] to match the production data from the Eagle Ford shale. In Yu's work [23], a similar method was used to match the production data from Barnett Shale and Marcellus Shale. The numerical techniques represent the state-of-the-art in history match and prediction of shale reservoir, but they are usually time and computing resource consuming [16], and require data and information which are not available in all wells [18].

From the review above, it can be concluded that when applied to the case of shale gas production, both approaches are not working well: the mathematical approach has better applicability but would bring huge errors because of lacking the physical background, on the other contrary the physical approach can obtain a good result but cannot be widespread used because of its complexity.

Previous studies have shown that the reservoir properties such as the initial gas distribution have significant impacts on the gas production [18,23–25]. In common, the gas exists as three major forms in shale reservoir: (1) free gas in big pores, fractures and nanopores, (2) adsorbed gas on the nanopores surface, (3) dissolved gas in kerogen/

clay and water [24,26,27]. Various methods are proposed to calculate initial gas distribution in unconventional gas area. In Ross and Bustin [28] viewpoint, only free gas flows at the early stage until the reservoir pressure is depleted to CDP (critical desorption pressure). Yang and Li [29] incorporated an artificial component subdivision in their numerical simulator to investigate the behavior of the original free gas and the adsorbed gas. Only distinguishing free gas and adsorbed gas is insufficient for shale reservoir due to its high heterogeneous properties. Etminan [30] developed a batch pressure decay (BPD) method to simultaneously measure the shale gas capacity from each source based on the distinctive changing of pressure decline curve slope. Javadpour [31] developed a method to calculate the gas diffusion coefficient in kerogen/clays offering an alternative way to calculate the proportion from each source.

In this study, a Gaussian Decomposition Method (GDM) is developed and applied to the prediction of shale gas production. The gas flow in the shale block is a multi-time, multi-scale and multi-physics process due to the diversity in minerals component and pore structure. GDM is proposed as an alternative approach to history matching and real-time prediction, and applied to decompose the evolving contributions of different gas components (free gas, adsorbed gas and dissolved gas), and applied to a spectrum of scales from laboratory scale to the field scale.

2. Development of a Gaussian Decomposition Method

2.1. Multi-time, multi-scale and multi-physics gas flow

Due to the ultra-low permeability, the horizon well and hydraulic fracture are the two essential processes for shale gas production. In this paper, the shale block defined as the shale matrix in the middle of the hydraulic fractures is investigated, shown in Fig. 1(a). As the SEM image shown (Fig. 1(b) [32]), the shale matrix is a typical porous medium which consists of nanotubes, kerogen and other minerals. The gas stores in the shale as (1) the free gas in nanotube, (2) the adsorbed gas on nanotube surface and (3) the dissolved gas in kerogen [3,57]. A cell tube can be used to characterize the heterogeneity of shale structure and gas storage as illustrated in Fig. 1(c) [26]. The gas flow in the

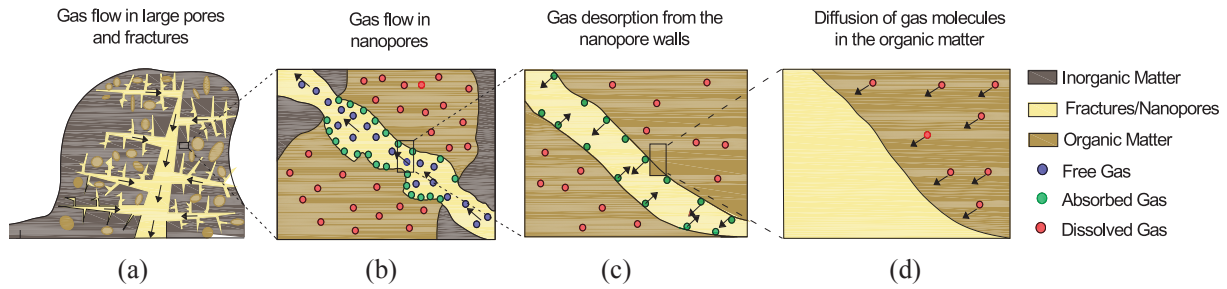


Fig. 2. Sequential depletion of shale gas: (a) Gas flow in big pores and fractures, (b) Gas flow in nanopores, (c) Gas desorption and (d) Molecules diffusion. The black arrows represent the gas flow direction.

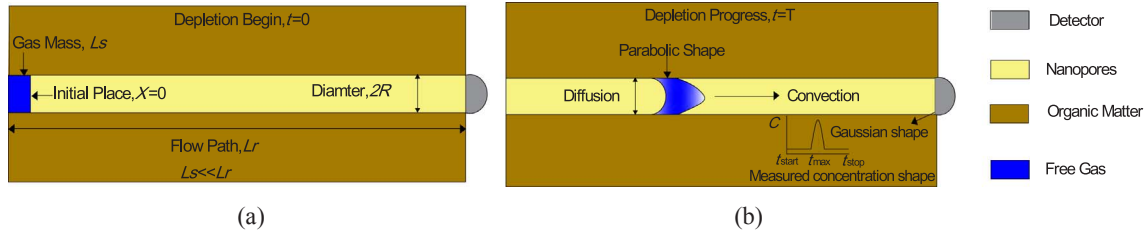


Fig. 3. The flow process of gas mass in nanopores during gas depletion process. (a) The initial state. R is the inner radius of sample tube, L_s is the length of gas mass, L_r is the length of flow path; At time $t = 0$, the gas mass is located at $x = 0$, and (b) the depletion process ($t = T$), the gas mass flows through a path of L_r and a parabolic-shape gradient forms within the nanotube.

Table 1
Initial value, lower and upper boundaries for moderate overlap [49].

Parameter	Initial Value	Lower boundary	Upper boundary
Retention time (b_0)	b_0	b_l	b_u
Standard deviation (c_0)	$\frac{((b_u - b_l)) + \sqrt{\ a_1 / a_2\ }}{2}$	$\min \left\{ \begin{matrix} b_u - b_0 \\ b_0 - b_l \end{matrix} \right\}$	$\max \left\{ \begin{matrix} b_u - b_0 \\ b_0 - b_l \end{matrix} \right\}$
Peak height (a_0)	$\frac{a_{0,max} + a_{0,min}}{2}$	$\min \left\{ \begin{matrix} a_1 \\ \left(\frac{b_u - b_l}{2} \right)^2 a_2 \end{matrix} \right\}$	$\max \left\{ \begin{matrix} a_1 \\ \left(\frac{b_u - b_l}{2} \right)^2 a_2 \end{matrix} \right\}$

shale block is a multi-time, multi-scale and multi-physics process due to the diversity in minerals component and pore structure. Once the production commences, the gas flow in shale block occurs in four sequential steps [31,33,34]. In the first step, the depleted gas is attributed to big pores and fractures present. The gas rate is usually high in this stage because of the high conductivity of the fractures but does not last long enough. Then, the free gas in nanopores moves toward the fracture or the big pores due to the gas pressure difference. In the third step, the

gas pressure drops leading the gas to strip from its adsorbed state on the nanopores surface to the free phase. Finally, the dissolved gas in kerogen/clay diffuses to the matrix-pore interface because of the concentration gradient between two systems. The sequential flow in shale reservoir is showed in Fig. 2.

The flow regimes and the associated probability density functions (PDFs) are varied with the storage term. The gas rate curve obtained from experiment or field is the superposition of different probability density functions (PDFs).

2.2. Probability density functions

Taking the depletion process of free gas in a nanopore as an example shown in Fig. 3(a), the gas mass having a length of L_s flows in the nanotube which has a length of L_r and a radius of R . There are three factors controlling the dispersion of the gas mass: 1. Axial diffusion due to the concentration gradient in axial direction; 2. Convective dispersion that changes the gas mass zone; 3. Radial diffusion due to the radial concentration gradient caused by the parabolic shape of gas mass. Some characteristics can be deduced: 1. The flow velocity u is

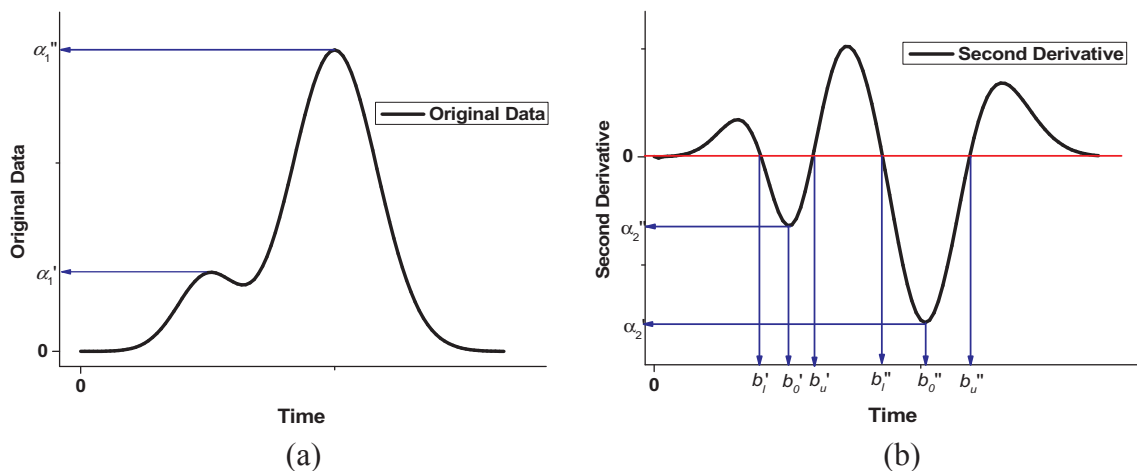


Fig. 4. The illustration and parameter meanings of (a) Moderate overlap curve and (b) second derivative curve.

Table 2
Initial value, lower and upper boundaries for strong overlap [49].

Parameter	Value	Lower boundary	Upper boundary
Retention time	b_0	b_l	b_u
Standard deviation	$\frac{((b_2 - b_1)) + \sqrt{\ a_1/a_2\ } + (t_2 - t_1) / 2n_4}{3}$	$\min \left\{ \begin{matrix} b'_2 - b_R \\ b_R - b'_1 \\ \sqrt{\ a_1/a_2\ } \end{matrix} \right\}$	$\max \left\{ \begin{matrix} b'_2 - b_R \\ b_R - b'_1 \\ \sqrt{\ b_1/b_2\ } \end{matrix} \right\}$
Peak height	$\frac{a_{0,max} + a_{0,min}}{2}$	0	a_1

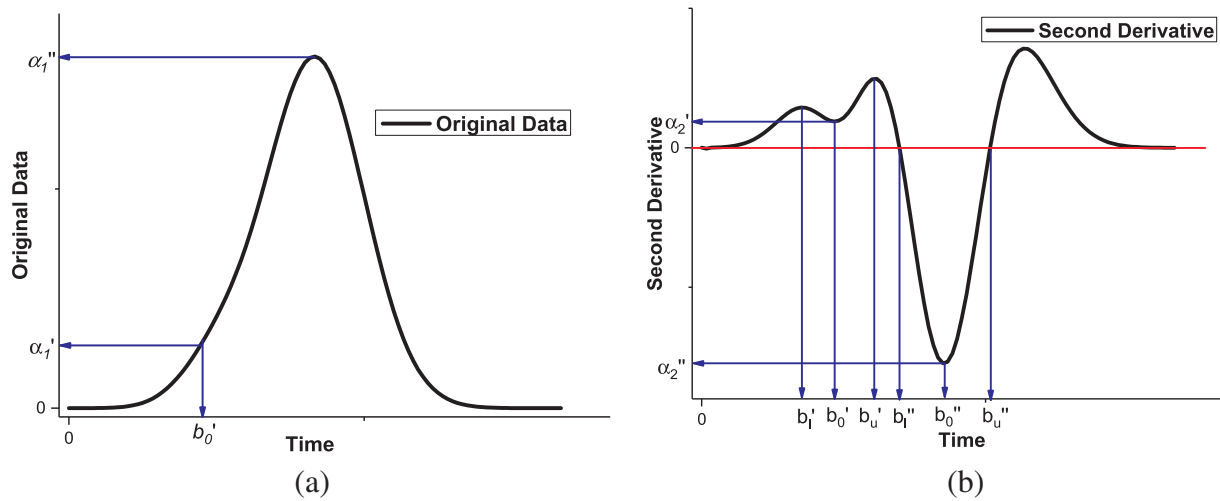


Fig. 5. The illustration and parameter meanings (a) strong overlap curve and (b) second derivative curve.

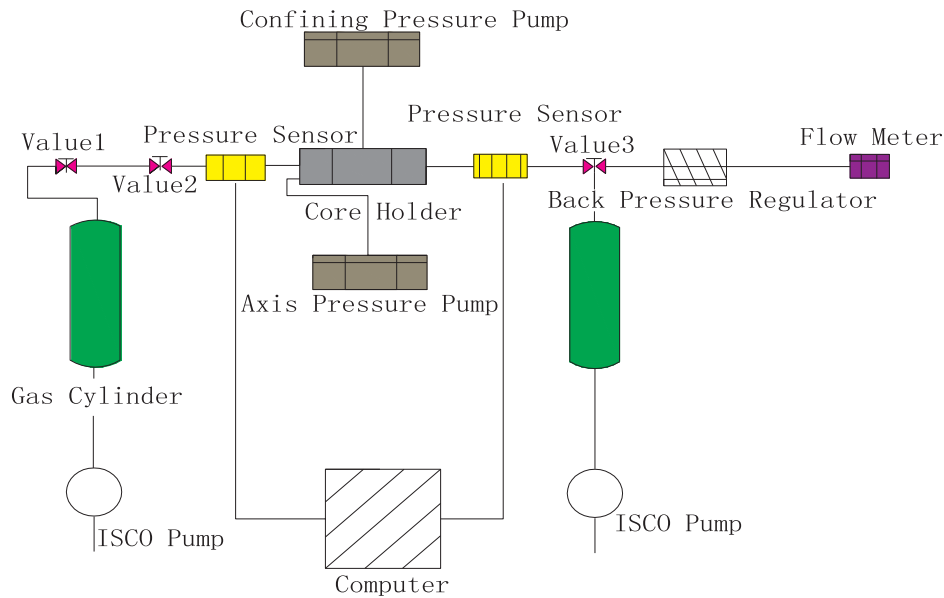


Fig. 6. Apparatus of coupled shale gas desorption-diffusion-flow experiment [58].

determined by the pressure gradient and permeability; 2. The Axial diffusion affect the gas mass shape 3. The concentration curve measured at the output is affected by the convection flow and axial diffusion, and some intrinsic properties can be inferred if the curve concentration at the detector is known.

The general equation of flow process is firstly investigated by Taylor [35,36] which can be written as:

$$D_m \left(\frac{\partial^2 C}{\partial r^2} + \frac{1}{r} \frac{\partial C}{\partial r} + \frac{\partial^2 C}{\partial X^2} \right) = \frac{\partial C}{\partial t} + 2U \left(1 - \frac{r^2}{R^2} \right) \frac{\partial C}{\partial X} \tag{1}$$

where the D_m is the molecular diffusion coefficient. For the case where the gas mass has a very small slug of length of L_s and the flow path L_r is relative long ($L_s \ll L_r$), the equation can be written as [37]:

$$\frac{\partial C}{\partial \theta} = \frac{1}{P_e} \frac{\partial^2 C}{\partial X^2} - \frac{\partial C}{\partial X} \tag{2}$$

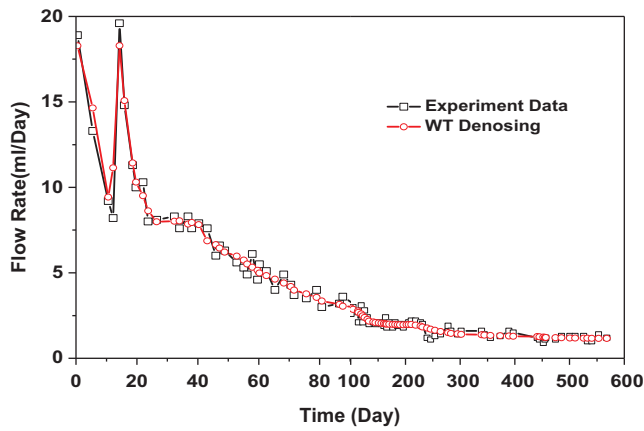


Fig. 7. The denoising result of experiment data from core sample.

where θ , X , C are the dimensionless time, axial distance and concentration, $P_e = uLr/D_m$ is the Peclet number which characterizes the dispersion properties of flow system. The general solution is [38]:

$$C = \frac{1}{2} \left\{ \operatorname{erf} \left[\frac{\theta - X}{2(\theta/P_e)} \right] + \operatorname{erf} \left[\frac{X + \alpha - \theta}{2(\theta/P)} \right] \right\} \quad (3)$$

where a is the dimensionless length of the initial gas mass. If the gas mass is very small compared to the tube volume which can be approximated by an ideal delta-function input, the solution is

$$C = \frac{1}{2} \left(\frac{P_e}{\pi\theta} \right)^{1/2} \exp \left[-\frac{P_e(X-\theta)^2}{4\theta} \right] \quad (4)$$

which has a Gaussian shape, shown in Fig. 3(b). The mean velocity is described by $U = \frac{Lr}{t_{max}}$ in which the t_{max} is the time when the maximum concentration occurs.

In our work, we assume that the displacement between initial places to the output occurs at a constant speed thus the X can be expressed as the liner function with time θ . Such assumption leads to the final expression of concentration which is written in the general form:

$$c(t) = ae^{-(t-b)/2c^2} \quad (5)$$

where a , b , and c are the curve parameters controlling the shape of the Gaussian function. a is the height of the curve at the maximum, b is the value of time where the maximum concentration occurs, and c controls the width of the curve. For the gas depletion process in field scale and experiment scale, the concentration curve measured at output is considered to be a mixture of several components whose concentration is given by Eq. (5). The total concentration at output is the sum of all the i-

Table 3
The initial values and lower/upper boundaries of parameters.

PDF		Gaussian Function Parameter		
		a_0	b_0	c_0
A	Initial Value	9.74	0	4.90
	Lower Boundary	1.20	0	0
	Upper Boundary	18.28	4	7.81
B	Initial Value	12.31	13.58	2.76
	Lower Boundary	6.32	13	0.58
	Upper Boundary	18.29	17	4
C	Initial Value	4.09	34.35	16.41
	Lower Boundary	0.15	31	3.35
	Upper Boundary	8.03	40	28.34
D	Initial Value	1.15	240	98.37
	Lower Boundary	0.30	190	50
	Upper Boundary	2.02	300	141.77

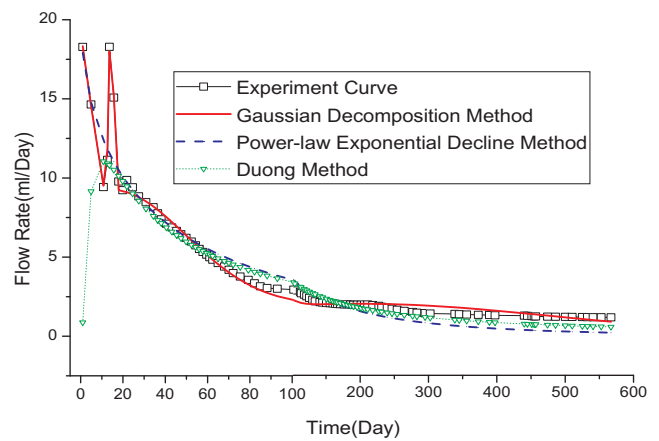


Fig. 9. Comparisons between different decline curves and the experimental data.

component:

$$c(t) = \sum_{i=1}^n a_i e^{-(t-b_i)/2c_i^2} \quad (6)$$

Practically, Javadpour [31] used the integral of Gaussian function to fit the gas desorption volume curve and obtained a good fitness. Mathematically, Goshtasby and Oneill [39] had proven that a sequence of spaced points with associated data values could be fitted by a sum of Gaussian function. In fact, the Gaussian function has been widely used

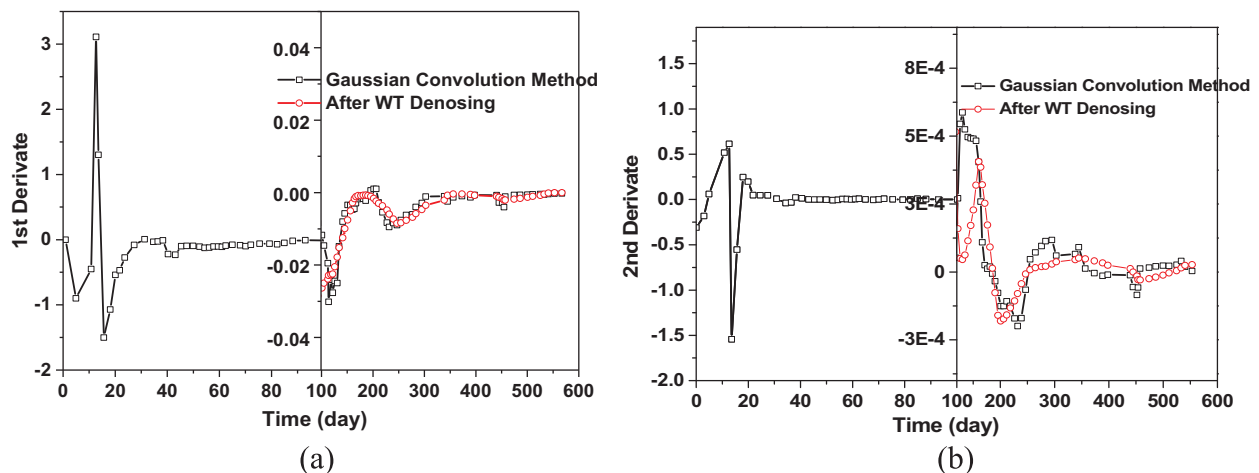


Fig. 8. The experiment data from core sample after (a) 1st derivative and (b) 2nd derivative.

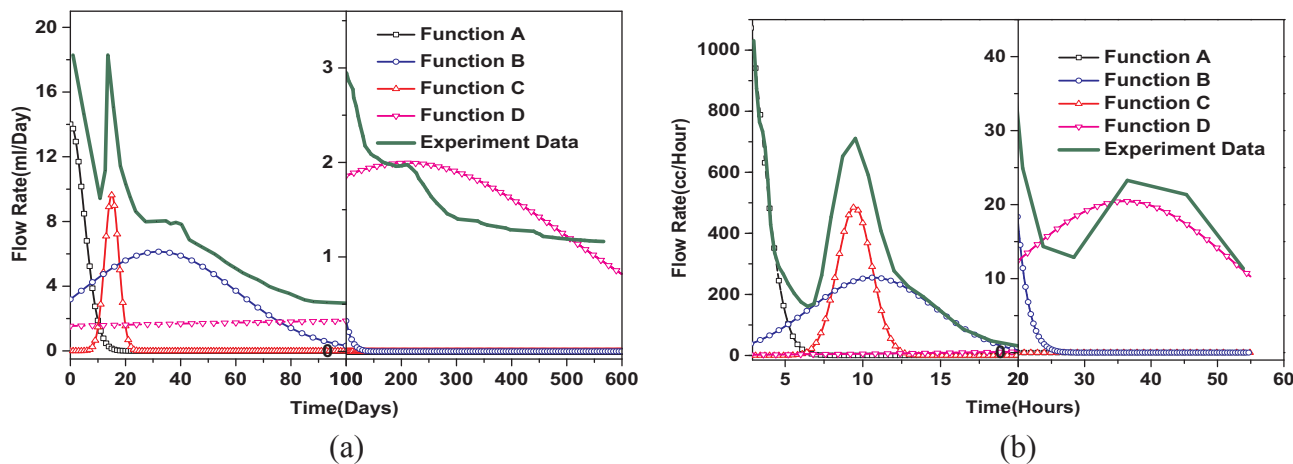


Fig. 10. Intensity of each PDF in (a) Guo's experiment and (b) Javadpour's experiment.

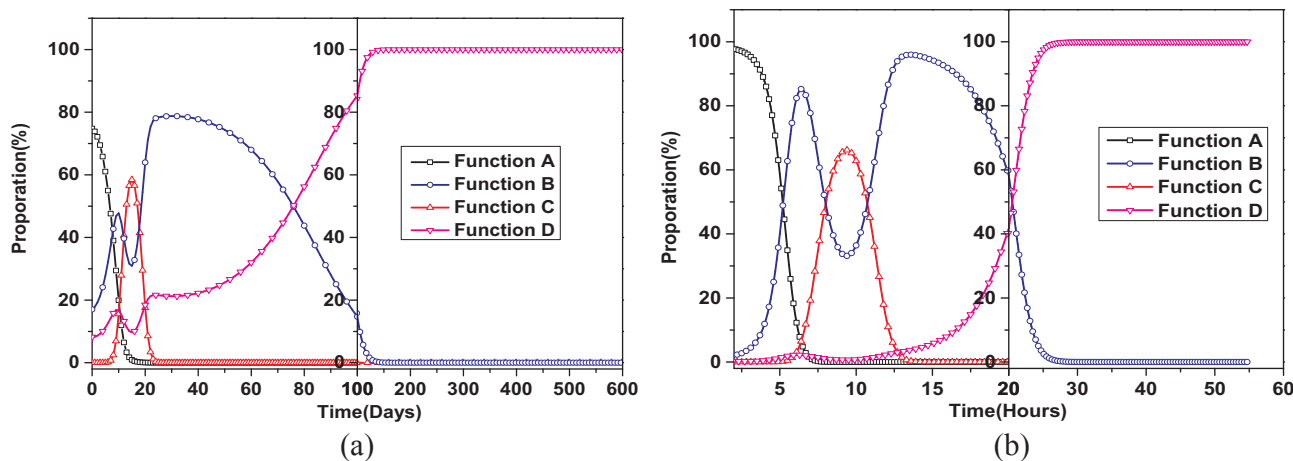


Fig. 11. The PDF proportions of (a) Guo's experiment and (b) Javadpour experiment.

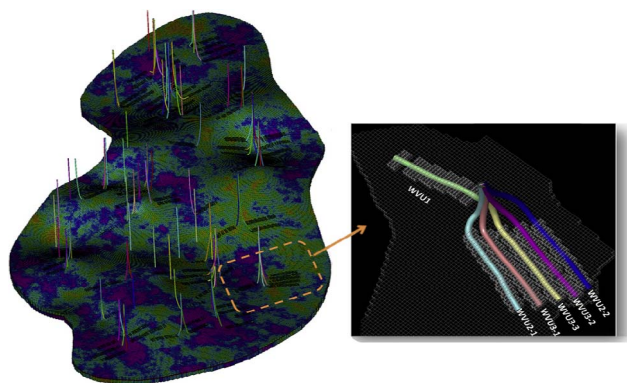


Fig. 12. A 3-D view of configuration of the target WVU pad.

in other fields such as flow injection analysis [40,41], chromatographic analysis [42] and thermal diffusion separation [43], and good results are obtained. Thus, the Gaussian function is selected as probability density function. The gas rate curve obtained from experiment or field is the superposition of different probability density functions (PDFs) and the flow regimes and the associated probability density functions (PDFs) are varied with the storage term. There are four probability density functions (PDFs) in this study: PDF A (gas flow in large pores and fracture), PDF B (gas flow in nanopores), PDF C (gas desorption from the nanopores walls) and PDF D (gas diffusion in the kerogen/clay).

2.3. Development of Gaussian Decomposition Method

In this section, a Gaussian Decomposition Method (GDM) is developed to get the expression of each PDF and the work flow of auto-compute program is introduced as follows.

2.3.1. Noise cancellation

The data obtained from experiment or filed is always contaminated by noises or errors and even small noises may lead to significant deviation in the data processing. The noises should be removed or reduced firstly before further processing [44]. The Wavelet Transform (WT) method is selected in our work because it works well for the analysis of non-periodic data [45,46]. After WT, the wavelet coefficient obtained from real data has a bigger amplitude than that obtained from noises. Based on that, an appropriate threshold on different scale is selected and suppress or eliminate the coefficient below the threshold. Finally, the denoised data is obtained through the inverse Wavelet Transform.

2.3.2. Data derivative

The data derivative is helpful for the case where the important information is hard to extract from the original data. In our work the data derivation especially the 2nd derivation is the basic of peak detection. The Gaussian Convolution method [47] is proposed to calculate the fractional order differentiation and also obtains a good result when applied to integer order differentiation. The process of Gaussian Convolution method is presented as follows.

The Gaussian convolution of data $c(t)$ can be presented as [48]:

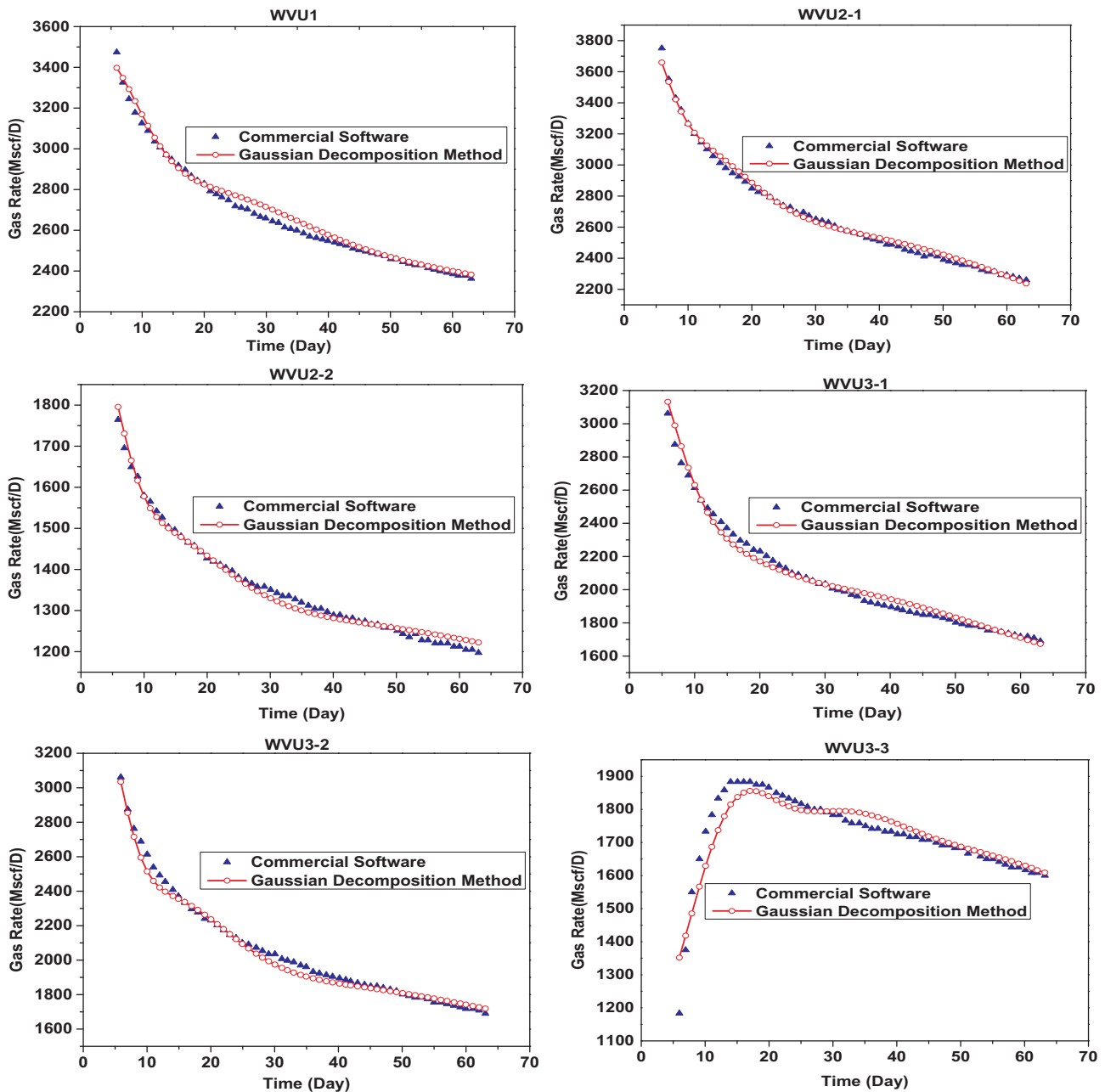


Fig. 13. Daily gas rate comparison of commercial software with GDM.

$$f(t) = c(t) * g(t) \tag{7}$$

where * denotes the convolution operation, $f(t)$ is the convolution result and $g(t)$ is the Gaussian function. Based on the property of convolution, the n th-order derivative of the data $s(t)$ can be computed as following:

$$f^{(n)}(t) = c^{(n)}(t) * g(t) = c(t) * g^{(n)}(t) \tag{8}$$

From Eq. (8), we notice that there is no difference whether the derivative operation is applied before or after the convolution.

According to the property of the order differentiation, there holds

$$c^{(v)}(t) = c^{(v_1+v_2)}(t) = c^{(v_1)} * c^{(v_2)}(t) \tag{9}$$

in which $v = v_1 + v_2$. Eq. (9) shows the v th-order derivative of the data $c(t)$ can be implemented by the v_2 th-order derivative of $c^{(v_1)}(t)$. This character gives us a method to calculate the 2nd or 3rd derivative based on the 1st derivative.

2.3.3. Initial iteration value determination

The identification of peaks and determination of the initial values (height a_i , centers b_i , tails c_i) for algorithm iteration are conducted with the derivative value. As mentioned above, the PDFs may overlap with each other thus a judgment criterion is proposed to determine whether a case is moderate overlap or strong overlap. A case would be classified as a moderate overlap situation, if the following condition is fulfilled and strong overlap if is not fulfilled:

$$n_3 \leq 2n_2 + 1 \tag{10}$$

where n_3 is the number of change in sign of the 3rd derivative and n_2 is the number of significant negative regions found in 2nd derivative. The determinations of initial iteration for moderate overlap and strong overlap require different ways.

2.3.3.1. Moderate overlap. Table 1 shows the calculations needed to obtain the initial values and the upper/lower boundaries for each

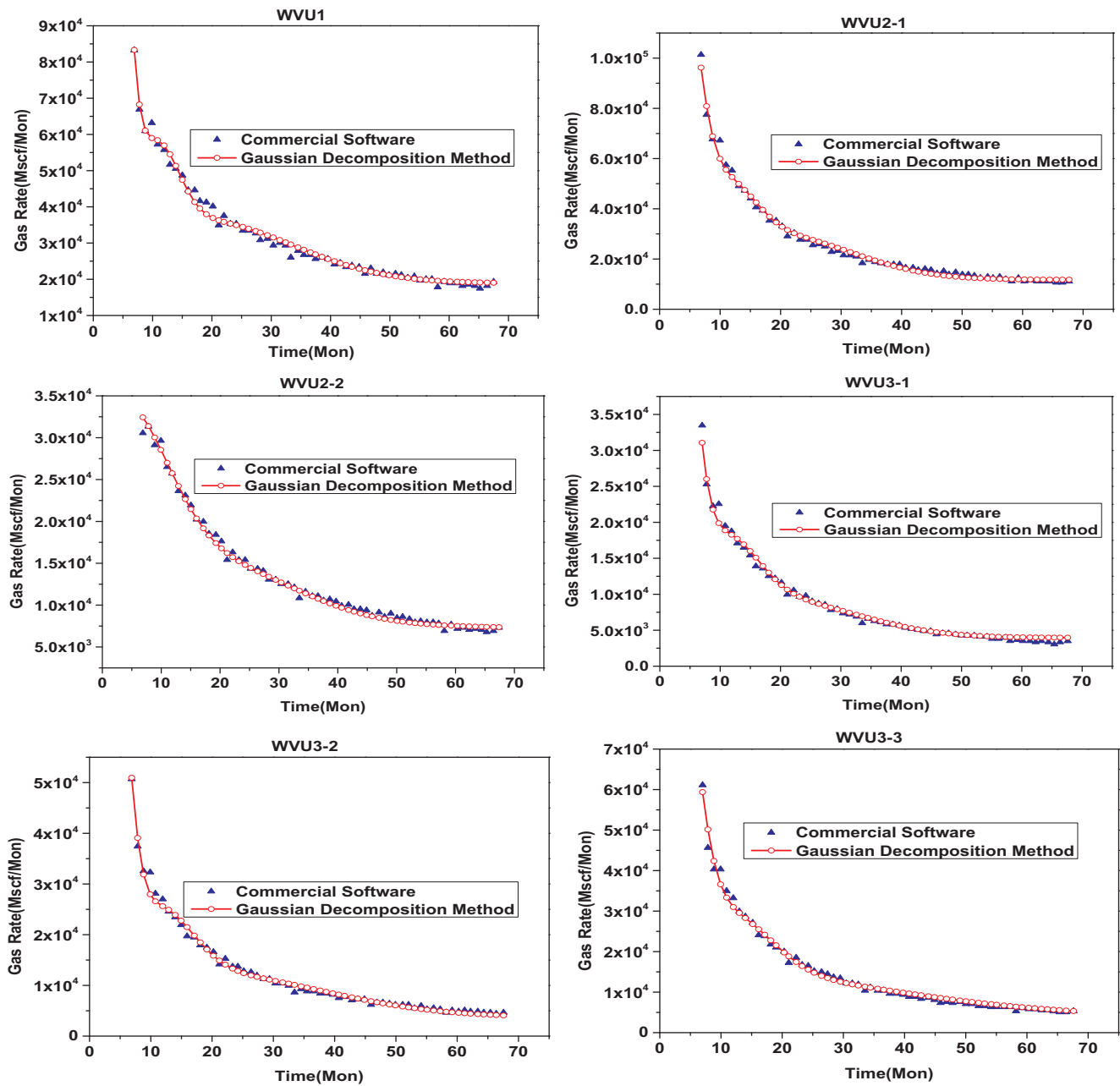


Fig. 14. Monthly gas rate comparison of commercial software with GDM.

parameter in the case of moderate overlap. Fig. 4 indicates the values of b_0, b_l, b_u, a_1 and a_2 . a_1 is the value of the input data at $x = b_0$, b_0 is calculated by finding the minimum of the second derivative, b_l and b_u are the times where the second derivative is zero, and a_2 is the value of the second derivative at $x = b_0$.

2.3.3.2. Strong overlap. Table 2 gives the calculation for each parameter of strong overlap case and Fig. 5 gives the value of each parameter needed for the calculation. The main modification is the inclusion of the approximation $(t_2 - t_1)/2n_4$, where n_4 is given by: $n_4 = ((n_c - 1)/2) + 1$, n_c is the number of changes in sign of third derivative in the time range where second derivative is negative, and t_2, t_1 are the time where second derivative is zero if it has the negative region.

2.3.4. Data fitting

The data fitting algorithm can be divided into two categories. One is

the traditional iteration method such as Levenberg–Marquardt method [50,51], Gauss–Newton method [52] and the other is recently developed stochastic optimization algorithm like Particle Swarm Optimization (PSO) and Ant Colony Optimization (ACO) [53,54]. In this work the Particle Swarm Optimization (PSO) algorithm is introduced which was first proposed by Kennedy and Eberhart [55,56].

Consider the following general unconstrained function optimization problem:

$$\begin{aligned} &\text{minimize } f(x_1, x_2, \dots, x_n) \\ &\text{where } f: R^N \rightarrow R \end{aligned} \tag{11}$$

The iteration for PSO algorithm is:

$$\begin{aligned} V_{id}(k+1) &= V_{id}(k) + \phi_{1d}(P_{id}(k) - x_{id}(k)) + \phi_{2d}(G_{id}(k) - x_{id}(k)) \\ x_{id}(k+1) &= x_{id}(k) + V_{id}(k) \end{aligned} \tag{12}$$

where $V_i = [V_{i1}, V_{i2}, \dots, V_{iN}]$ is the velocity for particle i ; $x_i = [x_{i1}, x_{i2}, \dots, x_{iN}]$ is the position of particle i ; ϕ_{1d} and ϕ_{2d} are uniformly distributed

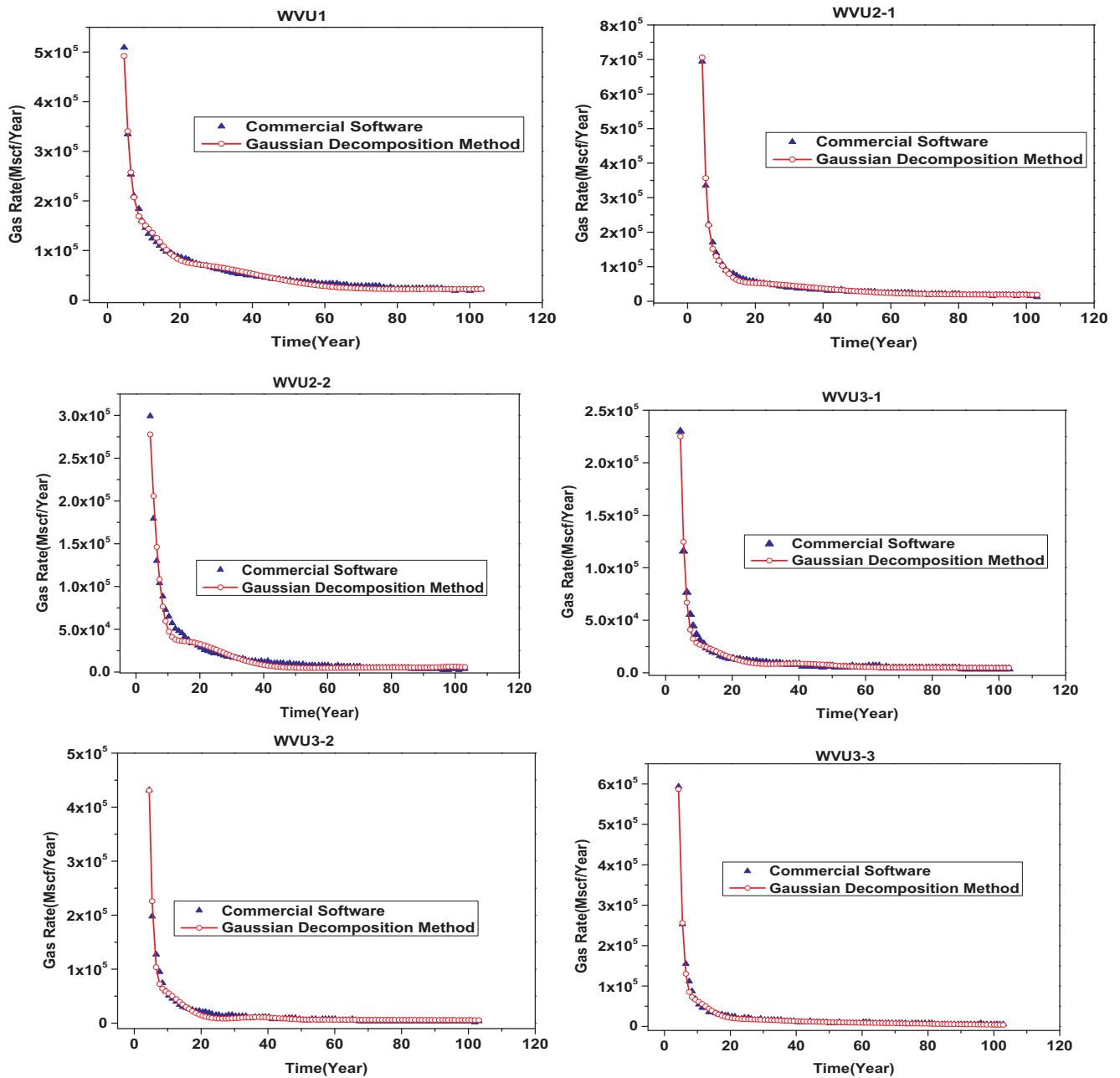


Fig. 15. Annual gas rate comparison of commercial software with GDM.

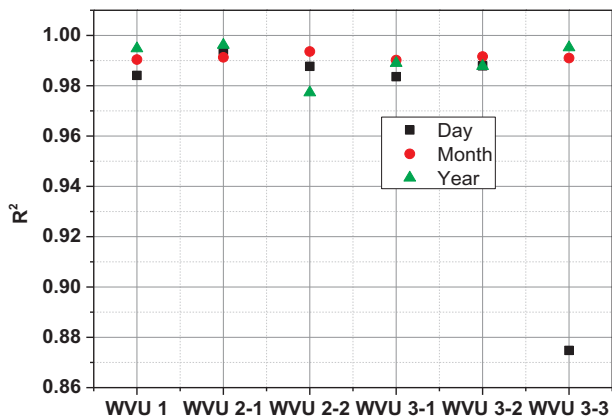


Fig. 16. The fitting correlation coefficient (R^2) of GDM at different time resolutions.

Table 4
Details of daily gas rate cases.

	Data Type	Time Span	Well Location	Well Tag	Fitting Goodness
Case 1	Daily	200 days	Marcellus shale	–	0.99
Case 2	Daily	20 years	Antrim Shale	–	0.97
Case 3	Daily	250 days	Eagle Ford	–	0.99
Case 4	Daily	800 days	Barnett Shale	Gas Well 1	0.96
Case 5	Daily	6 years	Barnett Shale	Gas Well 2	0.98
Case 6	Daily	7 years	Barnett Shale	Gas Well 3	0.83
Case 7	Daily	5.5 years	Barnett Shale	Gas Well 4	0.95
Case 8	Daily	6.5 years	Barnett Shale	Gas Well 5	0.96

Note: The case 8 differs from the previous examples in a way that the production data is collected two years later after well completion. In this case, the gas rate is composed by three Gaussian functions.

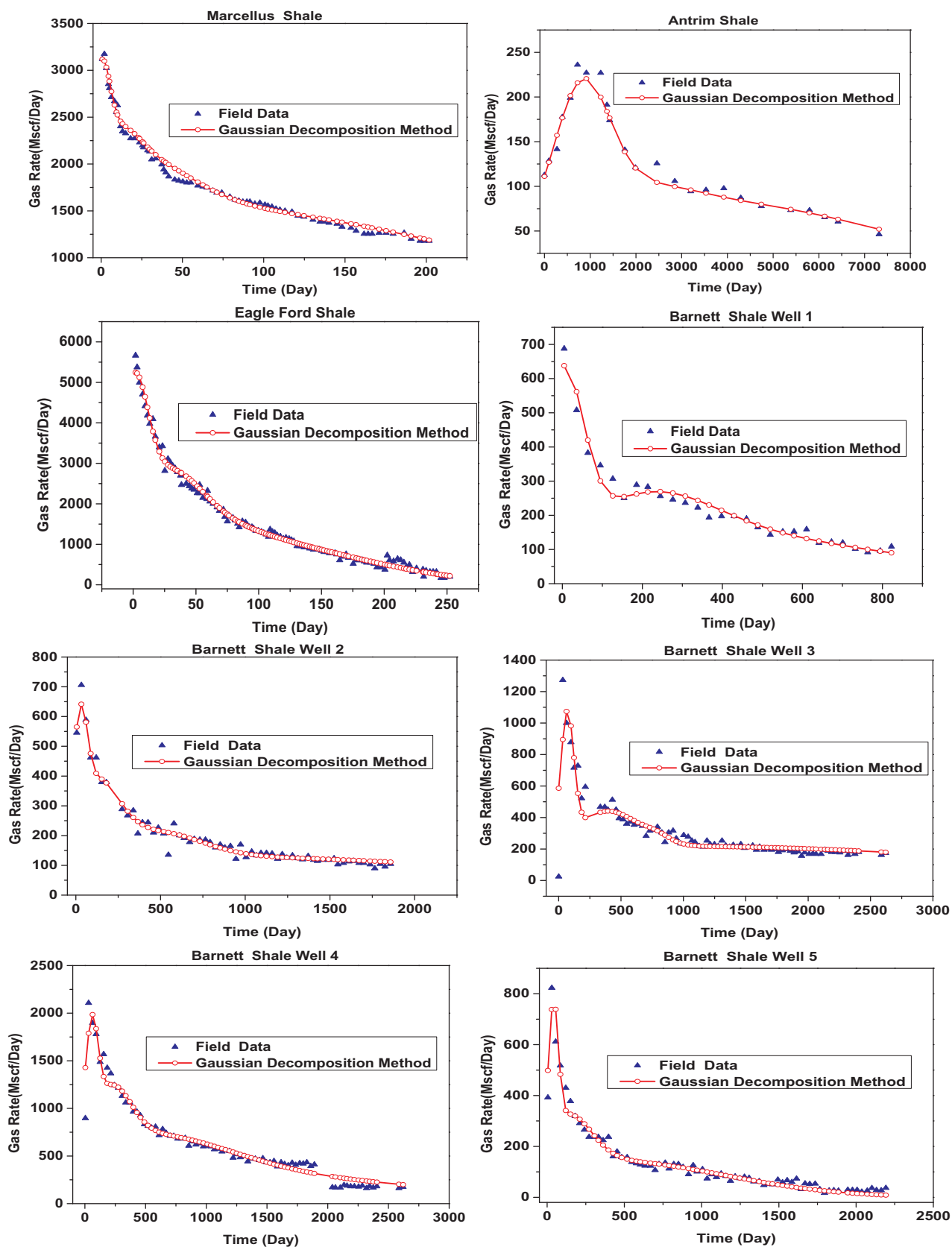


Fig. 17. Daily gas rate comparison-results from the field and GDM.

Table 5
Details of monthly gas rate cases.

	Data Type	Time Span	Well Location	Well Tag	Fitting Coefficient
Case 1	Monthly	40 months	Barnett shale	–	0.97
Case 2	Monthly	40 months	Fayetteville shale	–	0.99
Case 3	Monthly	37 months	Haynesville shale	–	0.98
Case 4	Monthly	43 months	Woodford shale	–	0.97
Case 5	Monthly	4 years	Marcellus Shale	#10125	0.97
Case 6	Monthly	2 years	Marcellus Shale	#10096	0.97
Case 7	Monthly	3 years	Marcellus Shale	#10103	0.95
Case 8	Monthly	2 years	Marcellus Shale	#10032	0.98

random number and generated independently for each dimension; $P_i = [P_{i1}, P_{i2}, \dots, P_{iN}]$ is the best position found by particle i ; $G_i = [G_{i1}, G_{i2}, \dots, G_{iN}]$ is the best position found by the entire population; N is the dimension of the search space and k is the iteration number. When a particle position is updated, the global best solution is replaced by the new solution if $f(x_i) < f(G_i)$. Thus, when a particle is updated, it has the opportunity to learn from all particles previously updated and this process results in a high convergence rate. The iterative process will continue until a stop criterion is satisfied, and this forms the basic iterative process of a standard PSO algorithm.

For the standard PSO algorithm, each particle position is random and the initial values of the entire best position are arbitrary [56,48] which easily lead to local optimal solution. To solve this, V_{id} is constrained to be bounded between V_{min} and V_{max} where V_{min} and V_{max} are the lower boundary and upper boundary calculated in the previous step, and the initial value obtained from the second derivative is set as the initial value of entire best position in PSO algorithm.

3. Application to core scale

3.1. Coupled desorption-diffusion-flow experiment

As demonstrated by other researches [18,23–25], the gas content and its initial distribution play an important role on the gas production performance. The measurement of gas content for shale reservoir can be conducted by using the desorption canister testing [57]. In this method, the gas content includes three portions: escaped gas, desorption gas and residual gas. However, the method has two shortages: (a) the escaped gas calculation would bring errors as it cannot be measured directly; (b) the residual gas measurement differs from the real gas production condition. Furthermore, the gas content obtained from the desorption canister testing is the Original Gas in Place (OGIP) rather than Technically Recoverable Resources (TRR).

A coupled gas desorption-diffusion-flow experiment was conducted to measure the TRR [58]. The core sample was collected from the lower Silurian Longmaxi Formation of Sichuan Basin, South China and the depth is 1048 m. The porosity is 0.4% and the permeability is about $2 \times 10^{-20} \text{ m}^2$. The experiment process was summarized as following: (1) Sample preparation. The sample was measured and put in the core holder; (2) Reservoir simulation. The axis and confining pressure were applied on the holder to simulate the formation pressure. Also, the methane gas cylinders were connected to both sides of holder to saturate sample. The saturation process lasted 240 days to make sure the fully saturation state; (3) Production simulation. The gas cylinders were removed when the core sample was fully saturated. Then a pressure drawdown was applied on the holder to simulate the gas production situation. The gas pressure and rate were recorded. The experiment apparatus is showed in Fig. 6.

3.2. Data analysis procedure

3.2.1. Noise cancellation result

Fig. 7 shows the comparisons of original data obtained from Guo's experiment with the denoising result conducted by WT. Obviously, the wavelet method is suitable for both the short period ($0 < T < 100$) and long period ($100 < T < 600$).

3.2.2. Data derivative result

Fig. 8 shows the results of 1st and 2nd derivative conducted by Gaussian Convolution method. The values between 100 and 600 days are strong oscillation and the WT is used again for denoising for long period ($100 < T < 600$).

3.2.3. Initial value determination and curve fitting results

In the following, the 1st and 2nd derivatives are used to determine the initial value and the lower/upper limit of the Gaussian function parameter as listed in Table 3.

The experiment data and the fitting results are shown in Fig. 9. For comparisons, we also use the Power-law Exponential Decline method [6,7] and Duong method [8] to curve fit the experiment data. The fitting curve generated by the Power-law Exponential Decline method decreases monotonically as shown in Fig. 9 and the fitting correlation coefficient is 0.9216. The fitting curve generated by the Duong method increases firstly then decreases as shown in Fig. 9 and the fitting correlation coefficient is 0.9736. While both methods cannot match the early data well because of the strong oscillation and the matching long-term data is lower than the experiment data. The fitting curve generated by the Gaussian Decomposition Method can match the whole-period data well and the fitting correlation coefficient is 0.9921.

3.3. Initial gas content distribution

The intensity of each PDF with time is showed in Fig. 10(a). PDF A, B, C and D represent the moving of free gas in the large pores/fractures, the flowing of free gas in nanopores, the desorption of adsorbed gas on the nanopores surface and the diffusion of dissolved gas in kerogen/clay, respectively. The experiment data in literature [31] are also processed for comparisons, showed in Fig. 10(b). The great discrepancy of two experiments is that in Javadpour's experiment the sample had already been cut into fragments before testing [31].

Two remarkable common points exist as shown in Fig. 10: (a) the function A is strong at first then falls to zero rapidly; (b) the function D is the only function existing in the last period. Two associated properties can be deduced: (a) the free gas in big pores/fractures moves out firstly and is characterized with high gas rate once the gas production commences; (b) the dissolved gas in kerogen/clay takes the full proportion of the last period.

The discrepancies exist in the early period of the gas flow process: the intensity of function D is zero for Javadpour's experiment while is not for Guo's experiment. Also, the intensity of function B in Javadpour's experiment is smaller than that in Guo's experiment. The reason may be that big pores/fractures were well connected in Javadpour's experiment as the sample was cut into pieces and the free gas were easily moving out compared with the intact sample in Guo's experiment.

The proportions of PDFs varying with time in both experiments are shown in Fig. 11. Two distinct features can be distinguished: the function A takes the great proportion in early period and the function D takes the full proportion in the last period. We can deduce that early period is the free gas in big pores/fracture dominant and the last period is the dissolved gas in kerogen/clay dominant.

The proportions of different gas storage terms to the whole volume are calculated. For Guo's experiment, the proportions of free gas in big pores/fractures (PDF A), free gas in nanopores (PDF B), the adsorbed gas on nanopores surface (PDF C), and dissolved gas in kerogen/clay

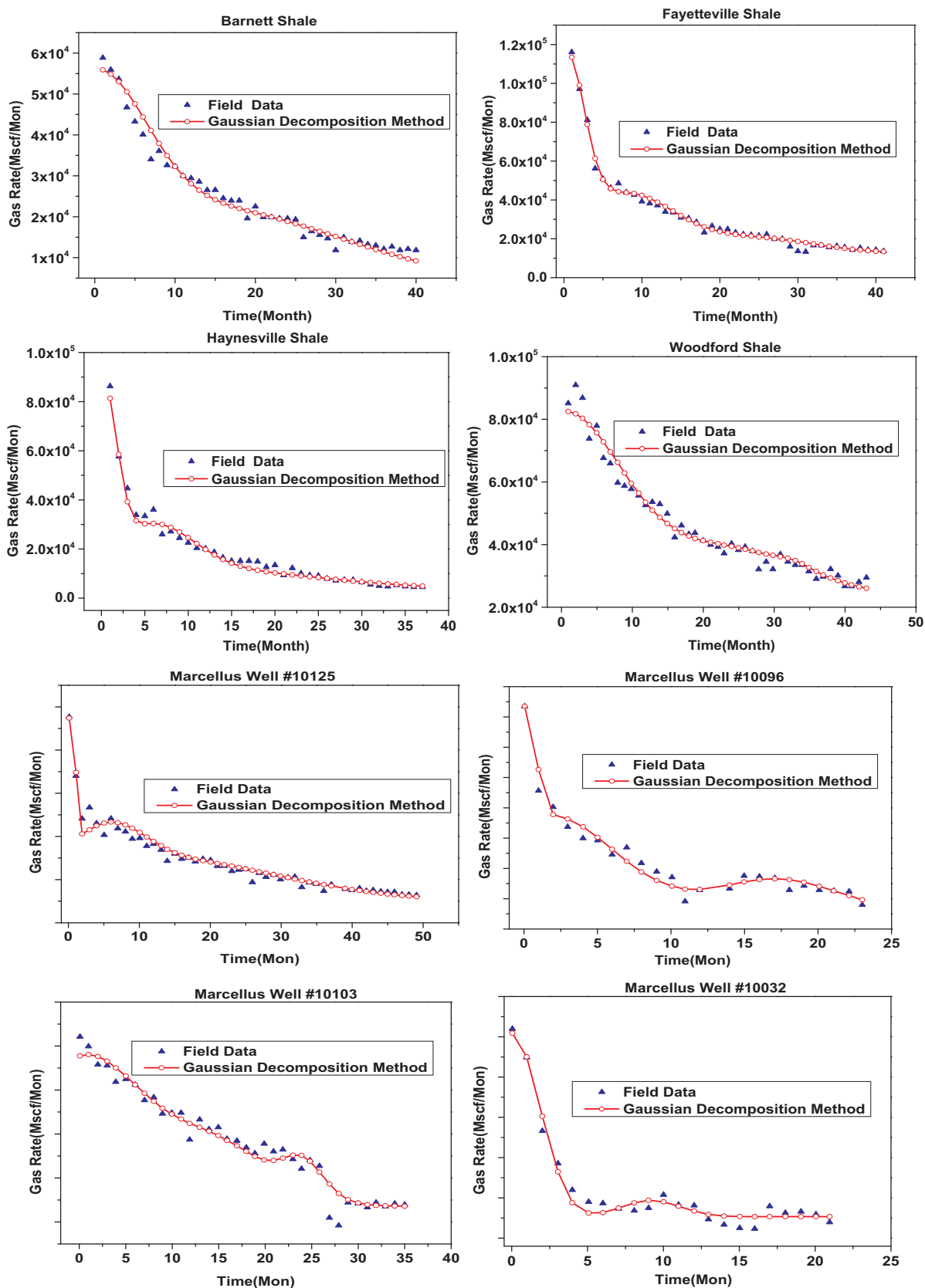


Fig. 18. Monthly gas production comparison-results from the field and GDM.

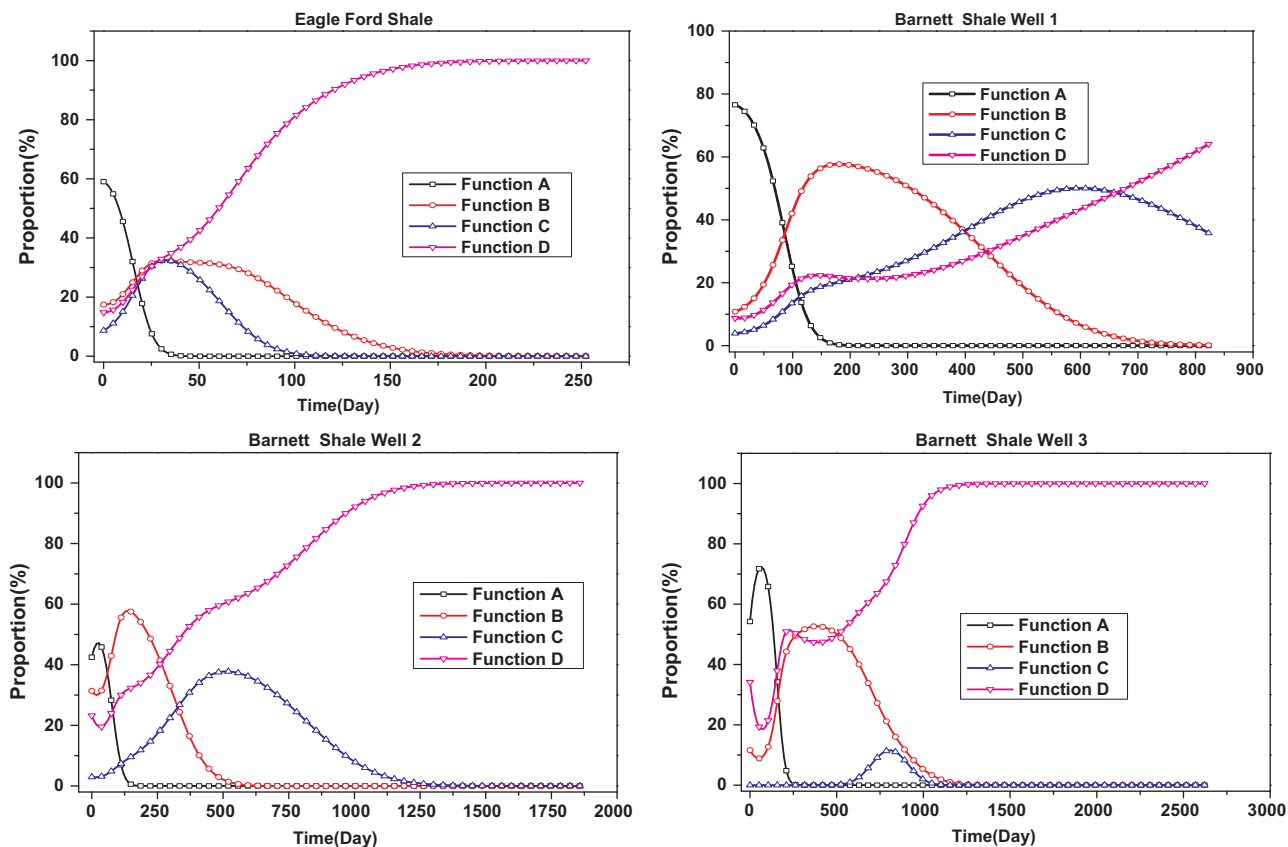


Fig. 19. The proportions of represented daily gas rate.

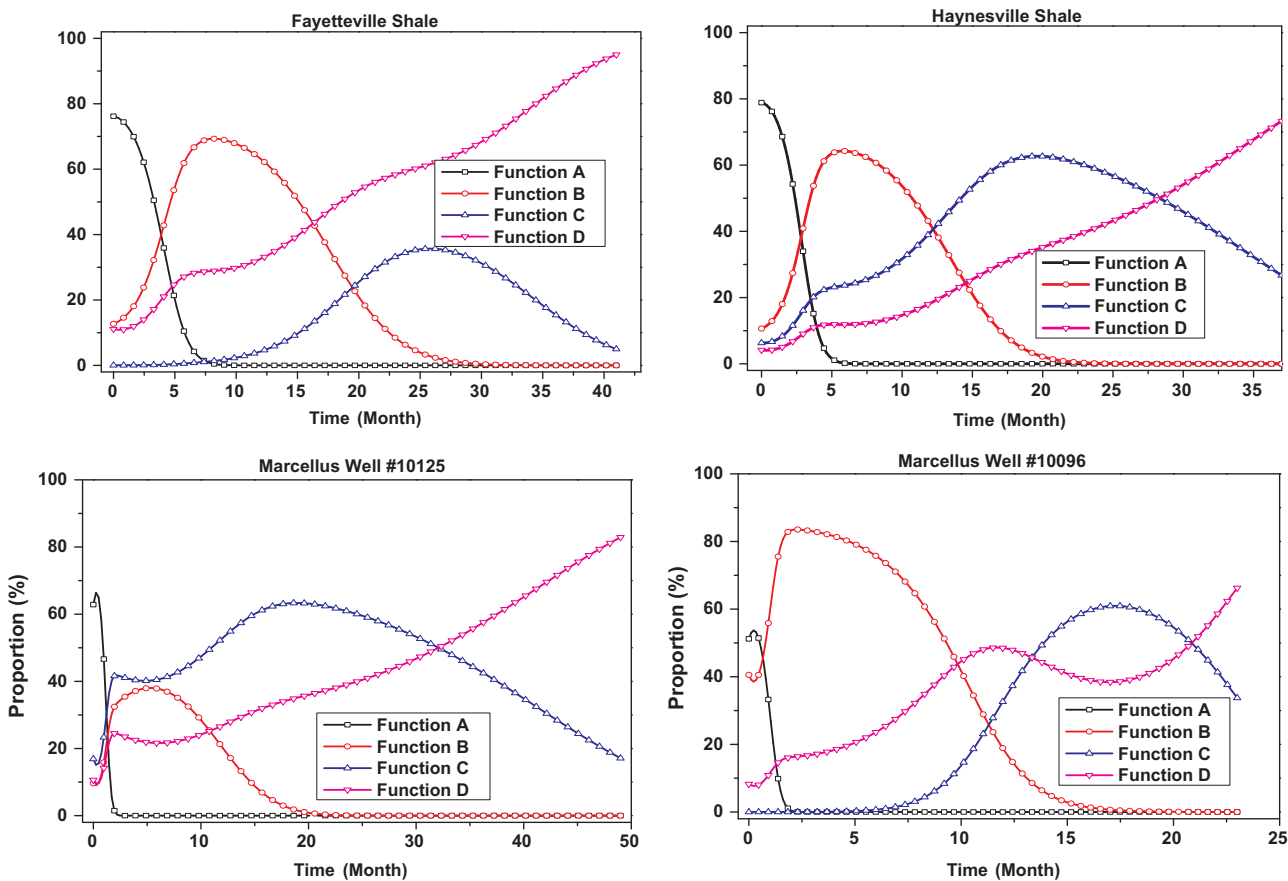


Fig. 20. Contributions of gas components to the monthly gas production rate.

Table 6
Proportion of each PDF.

Well Tag	Time Span	Proportion			
		Function A	Function B	Function C	Function D
Eagle Ford	250 days	0.11	0.21	0.14	0.54
Barnett Shale Well 1	800 days	0.17	0.31	0.26	0.26
Barnett Shale Well 2	6 years	0.06	0.17	0.14	0.63
Barnett Shale Well 3	7 years	0.12	0.18	0.01	0.69
Fayetteville shale	40 months	0.20	0.32	0.10	0.38
Haynesville shale	37 months	0.21	0.30	0.30	0.19
Marcellus Shale #10125	4 years	0.05	0.14	0.46	0.35
Marcellus Shale #10096	2 years	0.07	0.46	0.18	0.29

(PDF D) are 5.8%, 24.9%, 4.1%, 65.2% and for Javadpour’s experiment the values are 31.4%, 19.2%, 38.3%, 10.6%, respectively. The discrepancy is enormous. The reasons may be included but not limited to: (a) For the Javadpour’s experiment, the shale sample was cut into fragments and the equilibrium state was disturbed before measurement. During this process, gas in nanopores and kerogen/clay had moved into

big pore/fractures acting as free gas. (b) Long time is needed for the dissolved gas in kerogen/clay diffusion. But for Javadpour experiment, it only lasted 60 hours and most gas may be still in kerogen. For Guo’s experiment, it took almost 600 days and gas desorbed fully. In these two aspects, the Guo’s experiment is closer to the real shale production condition. (c) The geological condition difference may be another reason. Guo’s sample was collected from Sichuan Province in China and Javadpour’s sample was collected from North America.

4. Application to reservoir scale

4.1. Validation with commercial software

Three series of production data at hydraulic fracture level with different time resolutions (daily for the first two months, monthly for the first 5 years and annual for 100 years of production) developed by a commercial software in Kalantari-Dahaghi’s work [59] are used to fully verify the Gaussian Decomposition Method (GDM). In his work, one of the pads (called WVU pad) in Marcellus shale with six horizontal laterals is selected for verification and the location is showed in Fig. 12.

4.1.1. Daily gas rate

In all figures, the blue upper triangular dots represent the daily gas rate developed by a commercial software while the red lines with hollow circles represent the matching result from the GDM. Fig. 13 shows the examples of the comparison of commercial software simulation with the matched one by GDM. The fitting correlation coefficient

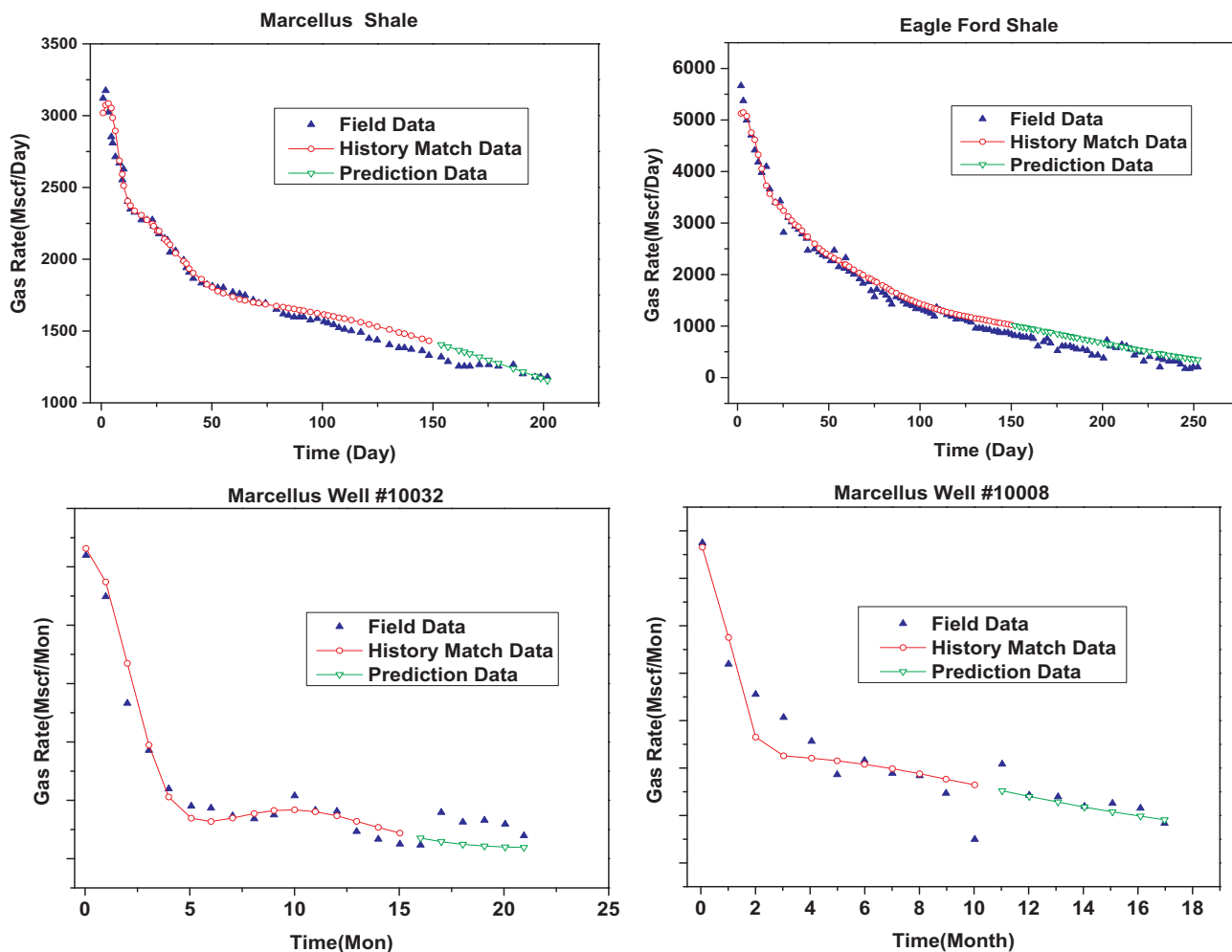


Fig. 21. The prediction results of short-term field data conducted by GDM.

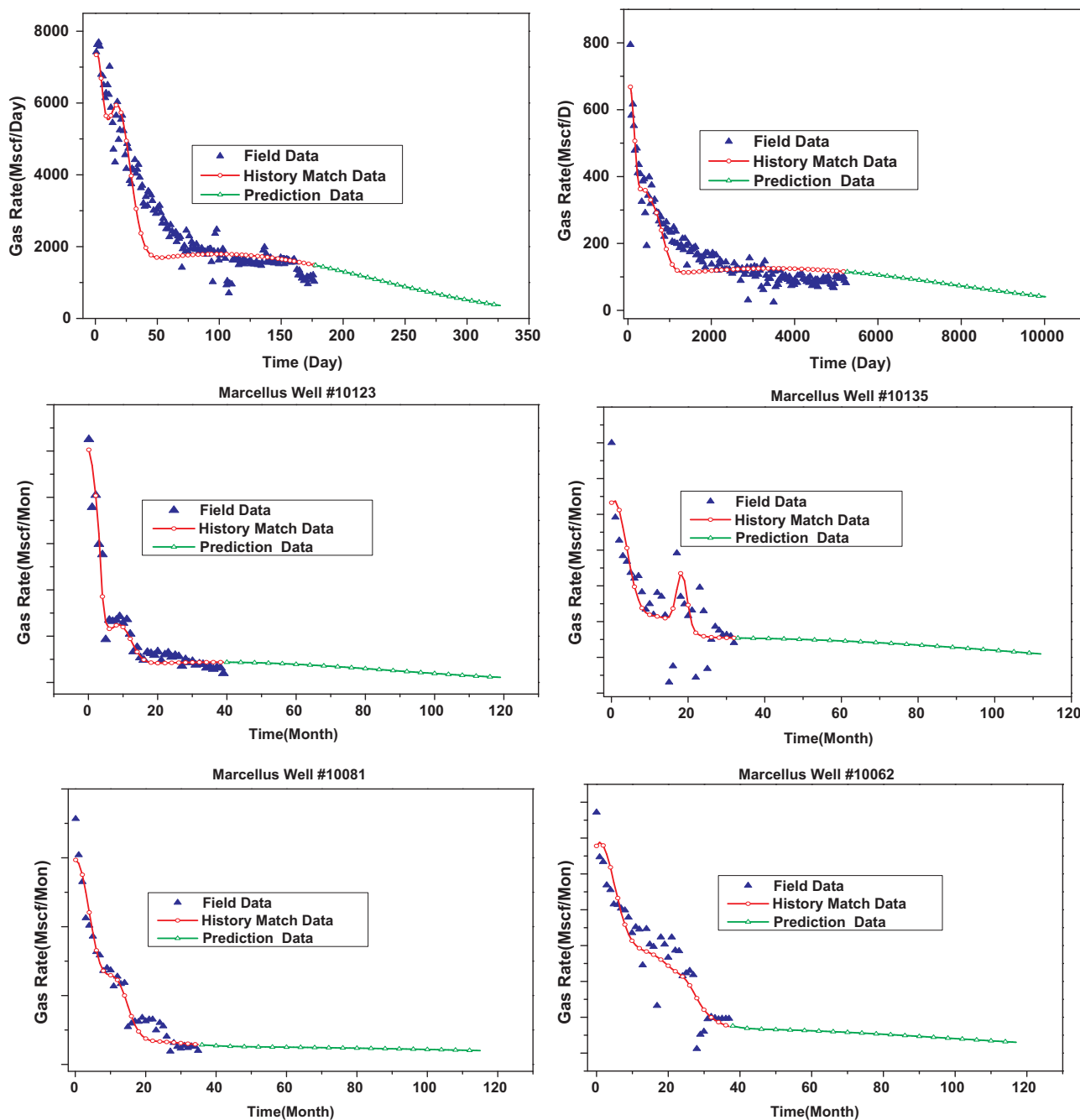


Fig. 22. The prediction results by using GDM.

(R^2) is shown as the black rectangle dots in Fig. 16. The results are self-descriptive enough to show the capability of GDM in the history match of daily gas production profile.

4.1.2. Monthly gas rate

Similarly, the monthly gas rate (Mscf/Mon) for the first five years in Kalantari-Dahaghi’s work [59] are used for the validation of GDM. Fig. 14 shows the comparison of commercial software simulations with results of GDM. In all cases, the fitting correlation coefficient (R^2) is above 0.99 (the red dot in [16]) indicating the successful application of GDM. The fitting result of monthly gas production data is better than that of daily gas production data.

4.1.3. Annual gas rate validation

The yearly gas rate profiles developed by the commercial numerical

simulator for the 100 years of gas production are successfully re-generated by GDM as showed in Fig.15 and the green upper triangular dots in [16]. As discussed above, the GDM plays well for verification of daily, monthly and annual gas rate. The only defect is that the GDM could not fully capture the case where the daily gas rate firstly increases then declines as the WUV3-3 case in Fig. 13.

4.2. History match with field data

In this section, the GDM is applied for the history match of the shale gas rate. Eight daily and monthly gas rates in literature [3,16,60,61] are presented.

4.2.1. History match of daily gas rate

Eight daily gas production rates from Marcellus shale [16], Antrim

shale [16], Eagle Ford shale [16] and Barnett shale [60] are history matched. The details are shown in Table 4.

The history match results and fitting correlation coefficients of eight cases are shown in Fig. 17 and Table 4. A good agreement is obtained. Among the eight cases, the case 6 (Well 3 of Barnett Shale) gets the poorest fitting correlation coefficient (only around 0.83) which is due to the fluctuation of early data. For other cases, the fitting correlation coefficients are greater than 0.95 indicating a good performance.

4.2.2. History match of monthly gas rates

Similarly, eight monthly gas rate cases from Barnett shale [3], Fayetteville shale [3], Haynesville shale [3], Woodford shale [3] and Marcellus shale [61] are history matched. The details are shown in Table 5. Here the dimensionless gas production rates of Marcellus shale reservoir are used.

The history match results and fitting correlation coefficients of monthly gas production rate are shown in Fig. 18 and Table 5, respectively. Generally, the fitting result of monthly gas rate is better than the daily data fitting result as the fitting coefficients are all above 0.95.

4.3. Contributions of different gas components

The contributions of different gas components to the whole quantity are also investigated by GDM. The evolving contributions of different gas components for represented daily and monthly gas rates are shown in Fig. 19 and Fig. 20, respectively. As illustrated above, PDF A, B, C and D represent the free gas in the large pores/fractures, the free gas in nanopores, the adsorbed gas on the nanopores surface and the dissolved gas in kerogen/clay.

Similar to the core scale analysis, two important properties can be deduced: (a) the free gas in the large pores/fractures takes great proportion during the early time but falls to zero rapidly; (b) the dissolved gas in kerogen/clay takes the significant proportion of the last period and if the time lasts long enough the dissolved gas will take full proportion.

The proportion of each PDF for the represented daily and monthly gas rate is shown in Table 6. Obviously, the proportion of each PDF is varied with the different geological conditions and the time span. The gas in big pores/fractures (Function A) takes small accounts in each well. For the same shale reservoir, the proportion of the dissolved gas in kerogen/clay (Function D) increases as production time continues.

4.4. Prediction of field gas production

4.4.1. Prediction of short-term field gas production

As discussed above, the GDM can match the data developed by the commercial software and the data obtained from field data. In this section, the GDM is applied to the prediction of field gas production. Firstly, the GDM is applied to the prediction of short-term field gas production. The process is conducted in two steps as follows: (1) the PDFs are calculated based on the existing production data; (2) the gas rate in next time period is predicted based on the calculated PDFs in first step. These two steps are repeated once the new production data is obtained. Two daily gas rates from Biswas [16] work, and two monthly gas rates from Esmaili [61] work are used for short-term gas rate prediction. In this section, the field data is divided into two parts: the first part is used to generate the probability density functions while the second part is applied to the comparison with the data obtained from GDM. The prediction results are showed in Fig. 21 and a good result is obtained.

4.4.2. Prediction of long-term field gas production

In this section, the GDM is applied to the prediction of long-term field gas production. Two daily gas rates from Clarkson [9] and Frantz [62] work, and four monthly gas rates from Esmaili [61] work are used for long-term gas rate prediction. The prediction results are shown in

Fig. 22 and a good result is obtained.

5. Conclusions

The conventional decline curve approaches cannot consider the unconventional multiple contribution mechanisms to the prediction of shale gas production. In this work, the Gaussian Decomposition Method (GDM) as an alternative is developed to overcome the shortcomings of the conventional decline curve methods. Based on the results of applications to both the core scale and the field scale, the following conclusions can be drawn:

- The unique features of multi-physics and multi-scale flow in shale gas reservoirs can be defined by a series of the Gaussian functions. Compared with other methods, the Gaussian Decomposition Method (GDM) can achieve better results for fitting the experiment data and field data, and GDM can calculate contributions of different gas components.
- When applied to the core scale, GDM can fit the desorption experiment curve and calculate the volume of each storage term. When applied to the reservoir scale, GDM can be used for both the history matching and the real-time prediction.

Acknowledgements

This work was funded partially by National Key R&D Program of China (No. 2016YFC0801401), National Natural Science Foundation of China (51504235; 51474204; 51609038), the 111 Project (B17009) and Yue Qi Distinguished Scholar Project of China University of Mining & Technology (Beijing). These supports are gratefully acknowledged.

References

- Johnson RH, Bollens AL. The loss ratio method of extrapolating oil well decline curves. *Trans AIME* 1927;77(1):771–8.
- Arps JJ. Analysis of decline curves. *Trans AIME* 1945;168:228–47.
- Fanchi JR, Cooksey MJ, Lehman KM, et al. Probabilistic decline curve analysis of Barnett, Fayetteville, Haynesville, and Woodford gas shales. *J Petrol Sci Eng* 2013;109:308–11.
- Valko PP. Assigning value to stimulation in the Barnett Shale: a simultaneous analysis of 7000 plus production histories and well completion records. In: *SPE hydraulic fracturing technology conference*, 19–21 January, The Woodlands, Texas, USA: SPE 119369; 2009.
- Valko PP, Lee WJ. A better way to forecast production from unconventional gas wells. In: *SPE annual technical conference and exhibition*, 19–22 September, Florence, Italy: SPE 134231; 2010.
- Ilk D, Perego AD, Rushing JA, et al. Integrating multiple production analysis techniques to assess tight gas sand reserves: defining a new paradigm for industry best. In: *CIPC/SPE gas technology symposium 2008 joint conference*, 16–19 June, Calgary, Alberta, Canada: SPE 114947; 2008.
- Ilk D, Rushing JA, Perego AD, et al. Exponential vs. hyperbolic decline in tight gas sands: understanding the origin and implications for reserve estimates using Arps' decline curves. In: *SPE annual technical conference and exhibition*, 21–24 September, Denver, Colorado, USA: SPE 116731; 2008.
- Duong AN. Rate-decline analysis for fracture-dominated shale reservoirs. *SPE Reserv Eval Eng* 2011;14(03):377–87.
- Clarkson CR, Williams-Kovacs JD, Qanbari F, et al. History-matching and forecasting tight/shale gas condensate wells using combined analytical, semi-analytical, and empirical methods. *J Nat Gas Sci Eng* 2015;26:1620–47.
- Stalgorova E, Mattar L. Practical analytical model to simulate production of horizontal wells with branch fractures. In: *SPE Canadian unconventional resources conference* 30 October–1 November, Calgary, Alberta, Canada: SPE 162515; 2012.
- Brown ML, Ozkan E, Raghavan RS, et al. Practical solutions for pressure transient responses of fractured horizontal wells in unconventional reservoirs. In: *SPE annual technical conference and exhibition*, New Orleans, Louisiana: SPE 125043; 2009.
- Ozkan E, Brown ML, Raghavan RS, et al. Comparison of fractured horizontal-well performance in conventional and unconventional reservoirs. In: *SPE western regional meeting* 24–26 March, San Jose, California, USA: SPE 121290; 2009.
- Apaydin OG, Ozkan E, Raghavan R. Effect of discontinuous microfractures on ultratight matrix permeability of a dual-porosity medium. *SPE Reserv Eval Eng* 2012;15(04):473–85.
- Dershowitz WS, Cottrell MG, Lim DH, et al. A discrete fracture network approach for evaluation of hydraulic fracture stimulation of naturally fractured reservoirs. In: *44th U.S. rock mechanics symposium and 5th U.S.-Canada rock mechanics symposium*, 27–30 June, Salt Lake City, Utah, USA: ARMA 10475;2010.

- [15] Fan L, Thompson JW, Robinson JR. Understanding gas production mechanism and effectiveness of well stimulation in the Haynesville shale through reservoir simulation. In: Canadian unconventional resources and international petroleum conference, 19–21 October, Calgary, Alberta, Canada: SPE 136696; 2010.
- [16] Biswas D. Shale gas predictive model (SGPM)—an alternate approach to model shale gas production. In: SPE eastern regional meeting 17–19 August, Columbus, Ohio, USA: SPE 148491; 2011.
- [17] Schepers KC, Gonzalez RJ, Koperna GJ, et al. Reservoir modeling in support of shale gas exploration. In: Latin American and Caribbean petroleum engineering conference 31 May–3 June, Cartagena de Indias, Colombia: SPE 123057; 2009.
- [18] Cipolla CL, Lolon EP, Erdle JC, et al. Reservoir modeling in shale-gas reservoirs. *SPE Reserv Eval Eng* 2010;13(4):638–53.
- [19] Yan B, Wang Y, Killough JE. Beyond dual-porosity modeling for the simulation of complex flow mechanisms in shale reservoirs. In: SPE reservoir simulation symposium, 18–20 February, The Woodlands, Texas, USA: SPE 163651; 2013.
- [20] Nejadi S, Trivedi JJ, Leung J. History matching and uncertainty quantification of discrete fracture network models in fractured reservoirs. *J Petrol Sci Eng* 2017;152:21–32.
- [21] Denney D. Fracture- and production-data integration with discrete-fracture-network models. *J Petrol Technol* 2000;52(12):60–1.
- [22] Doe T, Shi C, Enachescu C. Discrete fracture network simulation of production data from unconventional wells. In: Unconventional resources technology conference, 25–27 August, Denver, Colorado, USA: SPE 1923802; 2014.
- [23] Yu W, Sepehrnoori K. Simulation of gas desorption and geomechanics effects for unconventional gas reservoirs. *Fuel* 2014;116(1):455–64.
- [24] Passey QR, Bohacs K, Esch WL, et al. From oil-prone source rock to gas-producing shale reservoir – geologic and petrophysical characterization of unconventional shale gas reservoirs. In: International oil and gas conference and exhibition in China, 8–10 June, Beijing, China: SPE 131350; 2010.
- [25] Pan Z, Connell LD. Reservoir simulation of free and adsorbed gas production from shale. *J Nat Gas Sci Eng* 2015;22:359–70.
- [26] Javadpour F. Nanopores and apparent permeability of gas flow in mudrocks (shales and siltstone). *J Can Petrol Technol* 2009;48(8):16–21.
- [27] Cheng B, Liao Z, Wang T, et al. Multiple charges to Sinian reservoirs in the middle Sichuan basin, SW China: Insight from the adsorbed/occluded hydrocarbons in solid bitumens. *J Petrol Sci Eng* 2015;127:359–66.
- [28] Ross DJK, Bustin R. Impact of mass balance calculations on adsorption capacities in microporous shale gas reservoirs. *Fuel* 2007;86(17):2696–706.
- [29] Yang T, Li X, Zhang D. Quantitative dynamic analysis of gas desorption contribution to production in shale gas reservoirs. *J Unconventional Oil Gas Resour* 2015;9:18–30.
- [30] Etmian SR, Javadpour F, Maini BB, et al. Measurement of gas storage processes in shale and of the molecular diffusion coefficient in kerogen. *Int J Coal Geol* 2014;123:10–9.
- [31] Javadpour F, Fisher D, Unsworth M. Nanoscale gas flow in shale gas sediments. *J Can Petrol Technol* 2007;46(10):55–61.
- [32] Ambrose RJ, Hartman RC, Campos MD, et al. New pore-scale considerations for shale gas in place calculations. In: SPE unconventional gas conference, 23–25 February, Pittsburgh, Pennsylvania, USA: SPE 131772; 2010.
- [33] Peng Y, Liu JS, Pan ZJ, et al. A sequential model of shale gas transport under the influence of fully coupled multiple processes. *J Nat Gas Sci Eng* 2015;27:808–21.
- [34] Ghods P, Zhang D. Ensemble based characterization and history matching of naturally fractured tight/shale gas reservoirs. In: SPE western regional meeting, 27–29 May, Anaheim, California, USA: SPE 133606; 2010.
- [35] Taylor G. Dispersion of soluble matter in solvent flowing slowly through a tube. *Proc R Soc London Ser A* 1953;219:186–203.
- [36] Taylor G. Conditions under which dispersion of a solute in a stream of solvent can be used to measure molecular diffusion. *Proc R Soc London Ser A* 1954;225:473–7.
- [37] Kolev SD. Mathematical modelling of flow-injection systems. *Anal Chim Acta* 1995;308:36–66.
- [38] Kolev SD. Mathematical modelling of single-line flow-injection analysis systems with single-layer enzyme electrode detection Part I. Development of the mathematical model. *Anal Chim Acta* 1990;241:43–53.
- [39] Goshtasby A, Oneill WD. Curve fitting by a sum of Gaussians. *Graphical Models Image Process* 1994;56(4):281–8.
- [40] Quinn JG. Evaluation of Taylor dispersion injections: determining kinetic/affinity interaction constants and diffusion coefficients in label-free biosensing. *Anal Biochem* 2012;421:401–10.
- [41] Lewandowska A, Majcher A, Ochab-Marcinek A, et al. Taylor dispersion analysis in coiled capillaries at high flow rates. *Anal Chim* 2013;85(8):4051–6.
- [42] Daneyko A, Hlushkou D, Baranau V, et al. Computational investigation of longitudinal diffusion, eddy dispersion, and trans-particle mass transfer in bulk, random packings of core-shell particles with varied shell thickness and shell diffusion coefficient. *J Chromatogr A* 2015;1407:139–56.
- [43] Ryzhkov II, Stepanova IV. On thermal diffusion separation in binary mixtures with variable transport coefficients. *Int J Heat Mass Transfer* 2015;86:268–76.
- [44] Kharintsev SS, Kamalova DI, Mkh Salakhov, et al. Resolution enhancement of composite spectra using wavelet-based derivative spectrometry. *Spectrochim Acta A* 2005;61(1–2):149–56.
- [45] Rioul O, Vetterli M. Wavelets and signal processing. *IEEE Signal Proc Mag* 1991;8(4):14–38.
- [46] Donoho DL, Johnstone IM. Adapting to unknown smoothness via wavelet shrinkage. *J Am Stat Assoc* 1995;90(432):1200–24.
- [47] Li Y, Pan C, Meng X, et al. A method of approximate fractional order differentiation with noise immunity. *Chemometr Intell Lab* 2015;144:31–8.
- [48] Lin HC, Wang LL, Yang SN. Automatic determination of the spread parameter in Gaussian smoothing. *Pattern Recogn Lett* 1996;17(12):1247–52.
- [49] Vivó-Truyols G, Torres-Lapasio JR, Nederkassel AM, et al. Automatic program for peak detection and deconvolution of multi-overlapped chromatographic signals part I: peak detection. *J Chromatogr A* 2005;1096(1–2):133–45.
- [50] Ling C, Wang G, He H. A new Levenberg–Marquardt type algorithm for solving nonsmooth constrained equations. *Appl Math Comput* 2014;229:107–22.
- [51] Iqbal J, Iqbal A, Arif M. Levenberg–Marquardt method for solving systems of absolute value equations. *Appl Math* 2015;282:134–8.
- [52] Nadjiasngar R, Inggs M. Gauss-Newton filtering incorporating Levenberg–Marquardt methods for tracking. *Digit Signal Process* 2013;23(5):1662–7.
- [53] Xie W, Deng Z, Ding B, et al. Fixture layout optimization in multi-station assembly processes using augmented ant colony algorithm. *J Manuf Syst* 2015;37:277–89.
- [54] Sakthivel A, Vijayakumar P, Senthilkumar A, et al. Experimental investigations on Ant Colony Optimized PI control algorithm for Shunt Active Power Filter to improve Power Quality. *Control Eng Pract* 2015;42:153–69.
- [55] Eberhart R, Kennedy J. A new optimizer using particle swarm theory. In: Micro machine and human science, 1995. MHS '95, Proceedings of the sixth international symposium on, 4–6 October, Nagoya, Japan; 1995.
- [56] Eberhart RC, Shi Y. Particle swarm optimization: developments, applications and resources. In: Proceedings of the 2001, Congress on evolutionary computation, 27–30 May, Seoul, South Korea; 2001.
- [57] Shtepani E, Noll LA, Elrod LW, et al. A new regression-based method for accurate measurement of coal and shale gas content. *SPE Reserv Eval Eng* 2010;13(02):359–64.
- [58] Wei G, Zhiming H, Luo Z, et al. Gas desorption-diffusion-seepage coupled experiment of shale matrix and mathematic model. *Chin J Theor Appl Mech* 2015;47(6):916–22.
- [59] Kalantari-Dahaghi A, Mohaghegh S, Esmaili S. Coupling numerical simulation and machine learning to model shale gas production at different time resolutions. *J Nat Gas Sci Eng* 2015;25:380–92.
- [60] Mattar L. Production analysis and forecasting of shale gas reservoirs: case history-based approach. In: SPE shale gas production conference, 16–18 November, Fort Worth, Texas, USA: SPE 119897; 2008.
- [61] Esmaili S, Mohaghegh SD. Full field reservoir modeling of shale assets using advanced data-driven analytics. *Geosci Front* 2016;7(1):11–20.
- [62] Frantz JH, Sawyer WK, Macdonald RJ, et al. Evaluating Barnett shale production performance—using an integrated approach. In: SPE annual technical conference and exhibition, 9–12 October, Dallas, Texas: SPE 96917; 2005.